

ZnO/Nanocarbons-Modified Fibrous Scaffolds for Stem Cell-Based Osteogenic Differentiation

Yi Xia, Xin Fan, Hua Yang, Ling Li, Chao He, Chong Cheng,* and Rainer Haag*

Currently, mesenchymal stem cells (MSCs)-based therapies for bone regeneration and treatments have gained significant attention in clinical research. Though many chemical and physical cues which influence the osteogenic differentiation of MSCs have been explored, scaffolds combining the benefits of Zn²⁺ ions and unique nanostructures may become an ideal interface to enhance osteogenic and anti-infective capabilities simultaneously. In this work, motivated by the enormous advantages of Zn-based metal–organic framework-derived nanocarbons, C-ZnO nanocarbons-modified fibrous scaffolds for stem cell-based osteogenic differentiation are constructed. The modified scaffolds show enhanced expression of alkaline phosphatase, bone sialoprotein, vinculin, and a larger cell spreading area. Meanwhile, the caging of ZnO nanoparticles can allow the slow release of Zn²⁺ ions, which not only activate various signaling pathways to guide osteogenic differentiation but also prevent the potential bacterial infection of implantable scaffolds. Overall, this study may provide new insight for designing stem cell-based nanostructured fibrous scaffolds with simultaneously enhanced osteogenic and anti-infective capabilities.

1. Introduction

Because various degenerative bone diseases and inflammatory joint disturb many people all over the world, there is currently an urgent need for the supply of osteogenic and anti-infective scaffolds that provide bone regenerative therapies in the clinic.^[1–8] Mesenchymal stem cells (MSCs) are frequently investigated to differentiate to different kinds of cell lineage, including osteoblasts, they are considered as a good candidate for bone therapy.^[1,4,9–13] Meanwhile, MSCs' differentiation can be driven by the chemical and physical cues at material/cellular interfaces, thus providing a controllable protocol to manipulate the differentiation of MSCs without using complex bio-factors or cellular reprogramming processes.^[14–17] Indeed, chemical cues (metal ions, small molecules, and synthetic extracellular matrix) and phys-

ical cues (stiffness, micro-/nanotopography, and physical adhesion property) can efficiently influence MSCs' functionalities, including regulation of cell adhesion, proliferation, and differentiation.^[18–29] For instance, forces originated from the cell–material interface could change the cell membrane and subsequently affect the cell cytoskeleton, owing to the physical and mechanical interactions between the cells membrane the intracellular mechanoresponsive elements.^[20,30–33] Continuous immersion in Yes-associated protein (YAP) activation culture environments could decrease the human mesenchymal stem cells (hMSCs) multiple differentiation potency and promote osteogenesis.^[19,23]


Due to a variety of unique properties, carbon nanomaterials have been widely investigated as physical cues in tissue scaffolds to regulate stem cell behavior.^[22,34–40] For MSCs, it is suggested that carbon nanomaterials can provide binding sites with high stiffness to cell membrane receptors, and large adsorption and accumulation of nutrients,^[37,38] which may promote the fast formation of focal adhesion (FA). Then it triggers the rearrangement of F-actin and nuclear translocation of the YAP signal, finally improving the nuclear envelope protein Lamin A/C expression and activating the Runt-related transcription factor 2 (RUNX-2) pre-osteogenic marker expression, which eventually enhances the osteogenic differentiation.^[23,41–46] Among diverse kinds of carbon nanomaterials, the Zn-based metal–organic frameworks (MOFs)-derived nanocarbons (C-ZnO) have attracted much interest in the biomedical field.^[47] On the one hand, the large surface area and particular nanostructures of C-ZnO can facilitate the interactions between

Y. Xia, X. Fan, L. Li, Dr. C. He, Prof. C. Cheng
 College of Polymer Science and Engineering
 State Key Laboratory of Polymer Materials Engineering
 Sichuan University
 Chengdu 610065, China
 E-mail: chong.cheng@scu.edu.cn

Y. Xia, X. Fan, Prof. R. Haag
 Department of Chemistry and Biochemistry
 Freie Universität Berlin
 Takustrasse 3, Berlin 14195, Germany
 E-mail: haag@chemie.fu-berlin.de

H. Yang
 Institute of Mechanics
 Chair of Continuum Mechanics and Constitutive Theory
 Technische Universität Berlin
 Einsteinufer 5, Berlin 10587, Germany

L. Li
 Department of Ultrasound
 West China Hospital
 Sichuan University
 Chengdu 610065, China

 The ORCID identification number(s) for the author(s) of this article can be found under <https://doi.org/10.1002/smll.202003010>.

© 2020 The Authors. Published by Wiley-VCH GmbH. This is an open access article under the terms of the Creative Commons Attribution License, which permits use, distribution and reproduction in any medium, provided the original work is properly cited.

DOI: 10.1002/smll.202003010

the material and cell membrane.^[48–52] On the other hand, the Zn²⁺ ions do not only show strong inhibition on the growth of bacteria but also stimulate mineralization and osteoblast proliferation by improving anabolic influence on bone metabolism, thus promoting osteogenic differentiation of MSCs.^[51,53] Therefore, it is suggested that the C-ZnO-based nanocarbons that combine benefits of Zn²⁺ ions and unique nanostructures may become ideal candidates to construct favorable stem cells scaffolds with simultaneously enhanced osteogenic and anti-infective capabilities.

In this work, motivated by their advantages of Zn-based MOF-derived nanocarbons,^[47,52,54,55] we have constructed C-ZnO nanocarbons-modified fibrous scaffolds for stem cell-based osteogenic differentiation. Although ZIF-8 is size-morphology tunable and could contain multiple metal ions, they are not quite stable, especially in the acidic environment. Thus, the ZIF-8 nanostructure was carbonized and oxidized to obtain C-ZnO nanocarbons. The fibrous scaffolds were fabricated via electrospinning of a carrier polymer with C-ZnO nanoadditives. The expression of alkaline phosphatase (ALP) and bone sialoprotein (IBSP), and the calcium deposition test indicate that the engineered scaffolds show better osteogenic properties. The results of enhanced cell spreading area, vinculin expression, and F-actin rearrangement suggest the cell membrane and cytoskeleton sensed the physical cues of the nanostructured scaffolds. The following nuclear translocation of YAP, improved expression of Lamin A/C and RUNX-2 signaling emphasized the role of the C-ZnO in the regulation of cell–matrix interactions during promoting osteogenic differentiation. These detailed investigations confirm that the carbon nanostructures facilitate the adsorption and concentration of nutrients, which offer preferable environments for the growth and differentiation of MSCs. Meanwhile, the caging of ZnO nanoparticles can allow the slow release of Zn²⁺ ions, which not only activates various signaling pathways to guide osteogenic differentiation but also prevents the potential bacterial infection of implantable scaffolds. Overall, this study may provide new insight for designing stem cells-based nanostructured fibrous scaffolds with simultaneously enhanced osteogenic and anti-infective capabilities.

2. Results and Discussion

2.1. Preparation and Characterization of the C-ZnO Nanoparticles

ZIF-8 nanoparticles were prepared using 2-methylimidazole and Zn(NO₃)₂·6H₂O. Then, the ZIF-8 nanoparticles were then carbonized for 2 h at 800 °C with the protection of argon and oxidized for 2 h at 300 °C in air to obtain the C-ZnO nanoparticles (Figure 1a). Scanning electron microscopy (SEM) image in Figure 1b and the energy-dispersive X-ray spectroscopy (EDS) in Figure 1c suggest that C-ZnO nanoparticles are well prepared. Meanwhile, the size and morphology are relatively uniform and homogenous. Transmission electron microscope (TEM) image in Figure 1d exhibits that the sizes are around 50 nm. Moreover, the amplified high-resolution TEM in Figure 1e suggests that abundant ultra-small ZnO nanoparticles (yellow circles) homogeneously distribute on the carbon matrix. Figure 1f presents the high-angle annular

dark-field scanning TEM (HAADF-STEM) picture of C-ZnO and relative elemental mapping data, which proved the homogenous distribution of C, N, O, and Zn elements on nanocarbon. No big ZnO particles can be noticed from the images.

Further characterization of nanocarbons composition and chemical structure was performed by X-ray photoelectron spectroscopy (XPS) and the X-ray diffraction (XRD). The XRD in Figure 1g suggests that the ZIF-8 was successfully prepared. After carbonization and oxidation processes, no obvious peak for ZnO could be noticed, thus indicating that the ZnO doping provides amorphous structures. Moreover, the XPS survey scan in Figure 1h proved the existence of C, N, O, and Zn peaks. The high-resolution XPS C 1s spectra were fitted to four peaks (Figure 1i), which were corresponding to 288.0 eV (O=C–N, O=C–O), 286.5 (C=N, C=O), 285.1 (C–N, C–O), and 284.0 (C–C, C=C). The high-resolution XPS O 1s spectra in Figure 1j were fit to 532.9 (O–C), 531.6 (O=C), and 530.5 eV (O–Zn). As with previous report, Figure 1k shows two characteristic peaks at 1044.7 and 1021.7 eV in the Zn 2p spectra.^[54] Figure 1l suggests the measured atom ratio of C, N, O, and Zn are 62.04, 18.35, 12.55, and 7.04 at%, respectively. According to the data above, it is believed that C-ZnO nanocarbons were successfully synthesized.

Previous literature has already proven that poly(ϵ -caprolactone) (PCL) electrospun fibers were outstanding matrix for osteogenic tissue engineering.^[5,7,56] C-ZnO nanoparticles were incorporated into the fibrous scaffolds to investigate their interactions with hMSCs. As shown in Figure 2a, the obtained PCL/C-ZnO solutions were well dispersed and sucked into a syringe, then the fibers were collected on an aluminum foil when a certain voltage applied between the needle and substrate. As shown in Table S1 in the Supporting Information, the membrane scaffolds were prepared in hexafluoroisopropanol at the concentration of 10%, w/v PCL and 0%, 1%, 2%, and 5%, w/v C-ZnO nanoparticles.

To investigate the difference between bare ZnO nanoparticles and the C-ZnO, the ZnO-blended PCL (PCL-ZnO) with a similar amount of ZnO as that of PCL-ZnO-2 was fabricated. The morphology of the fibrous membrane is shown in Figure 2b and Figure S4 in the Supporting Information. The SEM data suggest that the fibrous scaffolds were composed of randomly overlaid fibers. The digital pictures of the prepared membrane suggest that after being mixed with C-ZnO nanoparticles, the color of the scaffold turns black. Meanwhile, with the increased concentration of the C-ZnO, the membrane scaffolds grow darker. As is shown on amplified SEM images, obvious C-ZnO nanoparticles could be observed on the fiber, which suggests that the C-ZnO nanoparticles were successfully blended into the fibers. The morphology of the scaffolds proved that the C-ZnO nanoparticles were uniformly distributed throughout fibers, and part of nanocarbons was observable on the fiber surface. As shown in Figure 2c, the diameter distribution of the prepared fibers suggests that after the concentration of nanocarbons reaches 2%, w/v, the fiber sizes decreased. The energy dispersive spectrometer data (EDS) and element mapping in Figure 2d,e suggest the abundant existence of Zn after the incorporation of C-ZnO nanoparticles. The water contact angle (WCA) in Figure S6 in the Supporting Information suggests that the pristine PCL fiber membrane is around 131.2°.

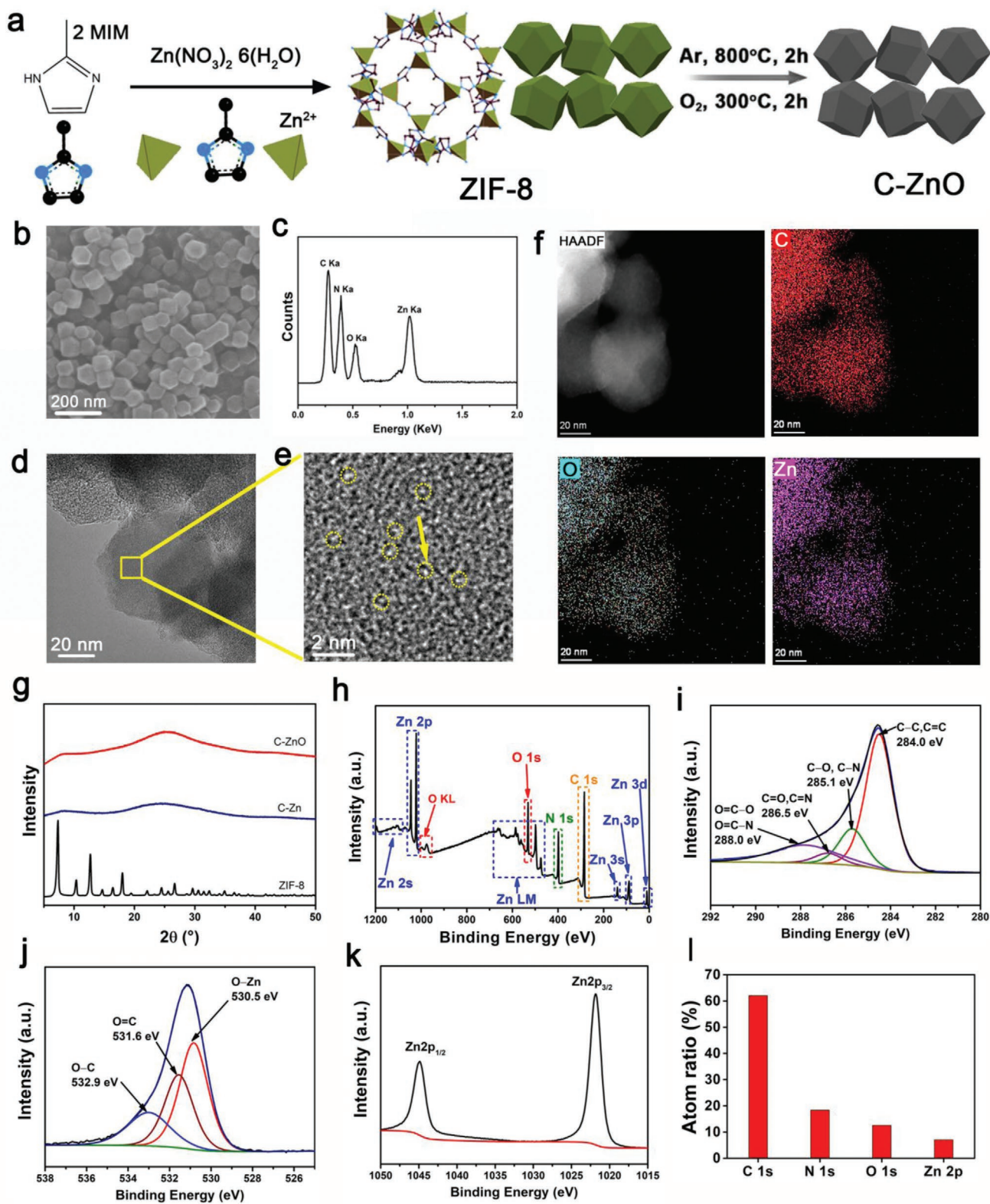


Figure 1. a) The ZIF-8 and C-ZnO preparation process scheme. b) Typical SEM image of the prepared C-ZnO nanoparticles. c) EDS curves of the C-ZnO particle. d) TEM image of the C-ZnO. e) High-resolution TEM image of the C-ZnO. f) HAADF-STEM image and elemental mapping of the C-ZnO. g) XRD spectra of ZIF-8, C-Zn, and C-ZnO nanoparticles. h) XPS survey scanning spectra for C-ZnO. The high-resolution XPS i) C 1s spectra, j) O 1s spectra, and k) Zn 2p spectra for C-ZnO. l) The atom percentages of C, N, O, and Zn in C-ZnO nanoparticles.

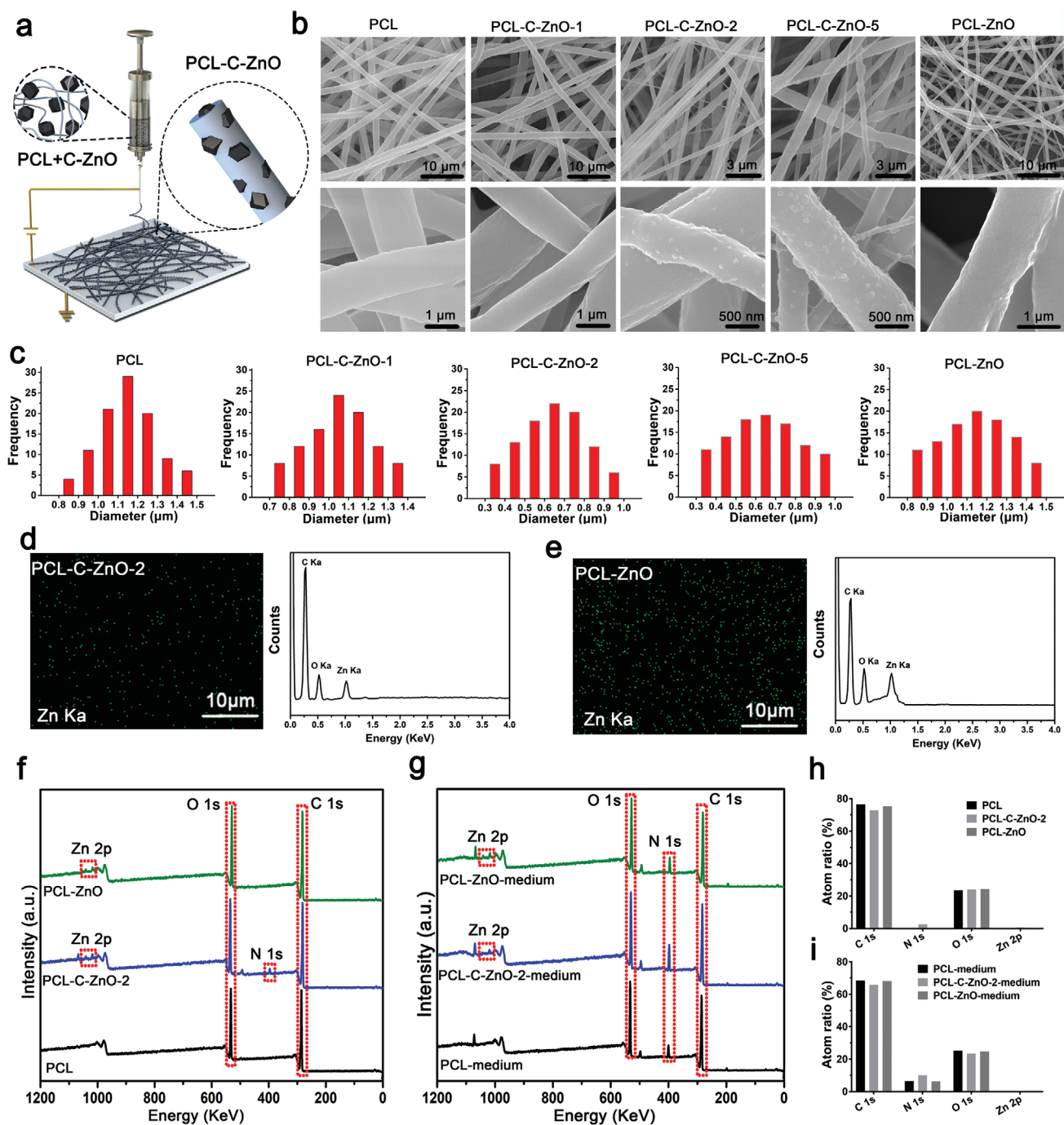


Figure 2. a) Schematic image for the preparation of PCL-C-ZnO nanofibrous scaffolds. b) SEM images for the electrospun bare PCL and PCL-C-ZnO scaffolds. c) The diameter distribution of the electrospun fibers ($n = 100$ fibers were quantified). d,e) The SEM element mapping and EDS curves of the PCL-C-ZnO and PCL-ZnO, respectively. XPS survey scanning spectra for f) fibrous scaffolds and g) cell culture medium immersed scaffolds. h) The atom percentages of C, N, O, and Zn on scaffolds and i) cell culture medium immersed scaffolds.

After the incorporation of C-ZnO nanoparticles, the WCA did not show any significant change between different samples.

To further prove the successful incorporation of C-ZnO and ZnO nanoparticles into PCL fibers, XPS was performed and exhibited in Figure 2f,h. According to the XPS survey scanning spectra, the nitrogen and zinc elements peaks indicate that the nanocarbons are successfully blended into the PCL-C-ZnO

fibers. Meanwhile, the zinc element on PCL-ZnO indicates that ZnO nanoparticles have been successfully coated into PCL fiber. After immersion in the cell culture medium, those contents of N 1s (Figure 2g,i) increased significantly compared to the original membrane nitrogen contents (Figure 2f,h). It is proposed that membranes could absorb diverse nitrogen-containing nutrients such as proteins, peptides, or amino acids

Table 1. Atomic compositions of the nanocarbon-incorporated PCL scaffolds before and after immersed in the cell culture medium, and the data are obtained from the XPS.

Sample	C 1s [%]	O 1s [%]	N 1s [%]	S 2p [%]	Zn 2p [%]	N/C ratio [%]
PCL	76.42	23.58	0	0	0	0
PCL-C-ZnO-2	72.92	23.91	2.56	0	0.6	3.51
PCL-ZnO	75.25	24.39	0	0	0.37	0
PCL-medium	68.37	25.17	6.46	0	0	9.45
PCL-C-ZnO-2-medium	65.68	23.43	10.14	0.31	1.34	15.44
PCL-ZnO-medium	68.19	24.69	6.35	0.28	0.48	9.32

from the media. As shown in **Table 1**, Compared to the pure PCL membrane, there is no apparent change in the content of N 1s on PCL-ZnO, which means the incorporation of ZnO nanoparticles could not improve the adhesion property. However, the higher content of N 1s on PCL-C-ZnO suggests that nanocarbons could contribute to a higher absorption amount of these nutrient molecules, which could exert beneficial effects on the MSCs growth and differentiation.

The MSCs proliferation activity and viability on the scaffolds were evaluated by cell counting kit-8 (CCK-8) analysis and lived/dead assay kit. The lived/dead cell in **Figure 3a** exhibits that the hMSCs are viable on all samples from the vertical pictures under the confocal microscopy after 3 days of culture. The statistical analysis of the cell numbers on the membrane in **Figure 3b** indicates that the live cell numbers on scaffolds did not change much after incorporation of C-ZnO nanoparticles until the concentration of 2%, w/v. However, the cell number on sample PCL-C-ZnO-5 decreased around 40% compared with pure PCL, which suggests that the increase of Zn²⁺ concentration exerted a negative effect on cell proliferation due to the potential oxidative stress caused by the ZnO.^[5] Meanwhile, all samples exhibited similar cell viability except PCL-C-ZnO-5 (**Figure 3c**). Additionally, the proliferation of hMSCs on scaffolds evaluated by a CCK-8 assay kit (**Figure 3d**) was similar to the results of the live/dead assay. On the first day, cells adhere well on all scaffolds; after 5 days of culture, the proliferation of cells on the PCL-C-ZnO-5 is less than PCL. Meanwhile, PCL-ZnO cell proliferation rate was less than PCL-C-ZnO-2 although the total amount of ZnO was the same, which indicated that the C-ZnO nanoparticles could reduce the release rate of Zn²⁺ ions, which may benefit the cell growth process. In summary, after incorporation of C-ZnO nanocarbons at the concentration of 2%, the hMSCs seeded on scaffolds could survive and proliferate much better than the other samples.

The osteogenic induction function of the scaffolds was further investigated in osteogenic induction media. The ALP expression at previous status was related to bone type matrix deposition, and the subsequent upregulation of other advanced osteoblastic markers was related to bone mineralization. Since the ALP activity is the strongest after 2 weeks of culture, ALP live staining after 14 days of culture was performed and observed with confocal microscopy, whereby the green fluorescence signal indicated the ALP activity. As shown in **Figure 3e**, ALP activity is the strongest on the surface of PCL-C-ZnO-2

compared with other samples. From the relative fluorescence intensity data in **Figure 3g**, it is evident that the incorporation of C-ZnO could improve the ALP expression in cells. Meanwhile, the lower ALP activity on PCL-C-ZnO-5 may mainly due to the fewer cellular metabolism activity compared with sample PCL-C-ZnO-2, which is following the results of cell proliferation. As the ALP activity on PCL-ZnO is less intense compared to PCL-C-ZnO-2, it indicates that the nanocarbon can promote the osteogenic induction as well.

We further used the ALP activity assay kit to quantify the osteogenic marker ALP expression on 7 and 14 days. As is shown in **Figure 3h**, the ALP activity increased after 2 weeks of culture compared to 1 week, which is in accordance with the literature.^[12,19] Meanwhile, the ALP activity on the sample PCL-C-ZnO-2 is also the strongest both at 7 days and 14 days. IBSP is an essential constituent in the bone since it is found to take part in around 8% of noncollagenous proteins in the bone extracellular matrix. The IBSP staining after 21 days is shown in **Figure 3f**; blue is DAPI (4',6-diamidino-2-phenylindole) and the green is the IBSP marker. The relative fluorescence intensity in **Figure 3g** suggests that the PCL-C-ZnO-2 exhibits the best performance compared with other samples. Calcium deposition amount of the MSCs is a significant landmark for the osteogenesis mineralization process, and we tested the calcium deposition on different samples after culturing for 14 and 21 days. **Figure 3i** suggests that the calcium deposition amount results are similar to the ALP and IBSP results. After incorporation of 2% C-ZnO nanocarbons into the fibrous structure, the ALP activity, IBSP expression, and calcium deposition were increased significantly compared with PCL and PCL-C-ZnO-5.

According to the biocompatibility test and osteogenic differentiation results, we found that the scaffolds with 2%, w/v C-ZnO nanocarbons presented the best performance compared with other samples. Therefore, PCL-C-ZnO-2 was chosen to perform the following osteogenic differentiation analysis. As is known that an extracellular matrix environment stimulates a series of cell signals reactions, which could modulate FA formation and cytoskeleton rearrangements. FAs and cytoskeleton protein on the cell-scaffolds interface play a pivotal role in cell motility, spreading, and differentiation via the FA kinase-signaling pathway. Confocal image of immunofluorescence staining with FAs protein (vinculin) and cytoskeleton protein (F-actin) is shown in **Figure 4a**. Blue is nuclear, red is F-actin, and the green represents the vinculin. It is shown that the cell spheroids exhibited highly spread morphologies on PCL-C-ZnO compared with pure PCL and PCL-ZnO. The cytoskeleton protein (F-actin) presents a linear microfilament structure, which supports the whole cell structure. The amplified F-actin (red) and vinculin (green) confocal images in **Figure 4b** suggest that the vinculin protein grows along the cytoskeleton microfilament, which is crucial during the cell spreading. As shown in the schematic illustration in **Figure 4c**, due to larger surface area and the corresponding more binding sites, the carbon nanomaterial structure on fibrous surfaces could improve cell adhesion. The vinculin intensity value along the white line is shown in **Figure 4d**, and the high-value peaks suggest the expression of vinculin protein, the cell vinculin expression signal on PCL-C-ZnO-2 is much more frequent and stronger than that on PCL and PCL-ZnO, which indicates that the incorporation of carbon

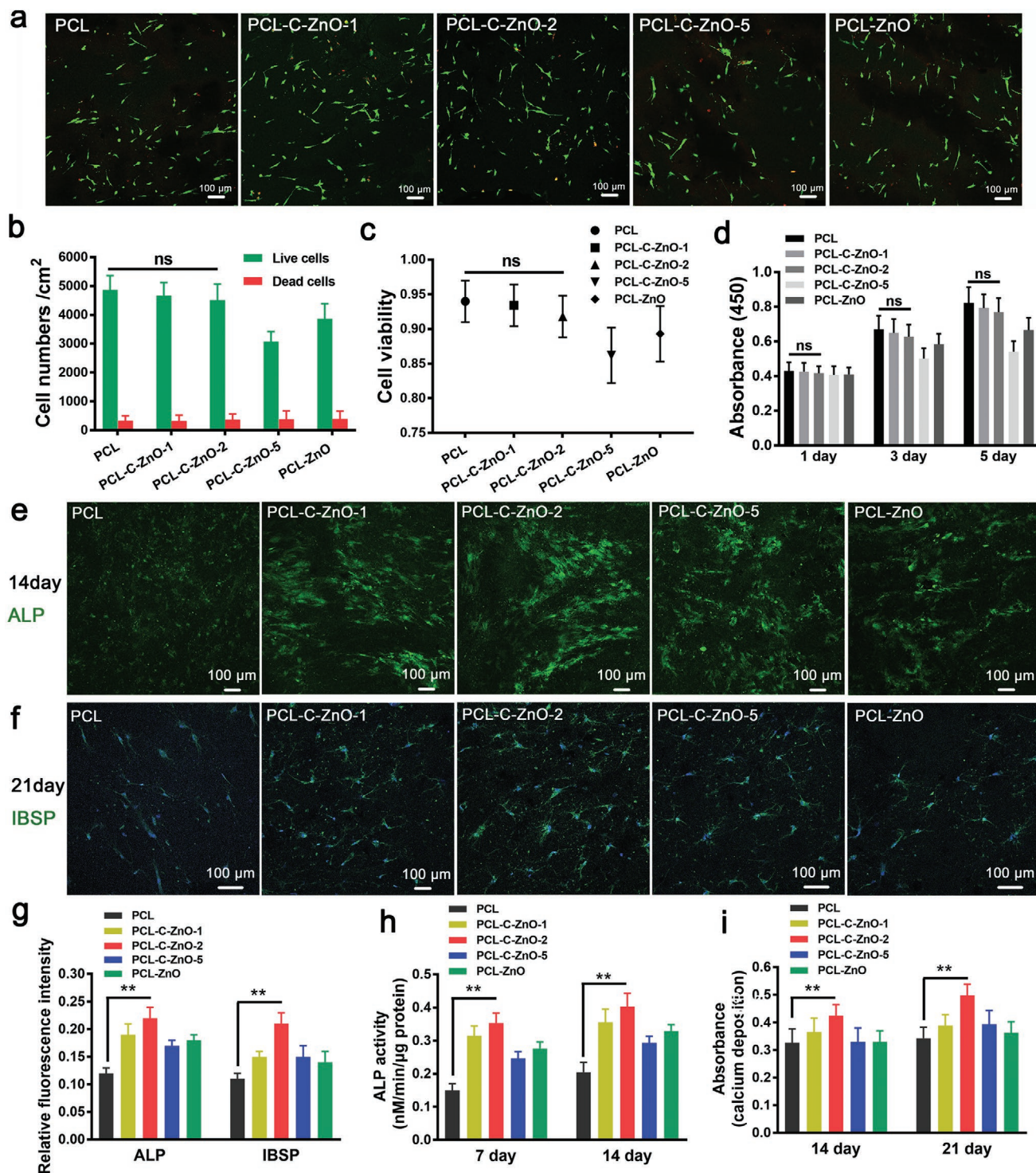


Figure 3. a) Confocal image of live/dead cells (green: live, red: dead) of hMSCs after seeding on different samples for 3 days. b) Quantitative analysis of cell numbers on the scaffolds from the confocal image after 3 days. Statistical quantification of the cell numbers on the surface, n is the number of confocal pictures analyzed (mean \pm SD, $n = 10$). c) Cell viability quantitative analysis according to the live/dead cell numbers (mean \pm SD, $n = 10$). d) The absorbance of live cells after 1, 3, and 5 days culture using the CCK-8 assay kit (mean \pm SD, $n = 6$). e) ALP live-staining of hMSCs after being incubated on the scaffolds for 14 days. f) Fluorescence staining image of mature osteogenic marker IBSP after 21 days of culture on scaffolds (blue is DAPI and green is IBSP). g) The average expressions of ALP and IBSP were quantified according to the fluorescence-stained image intensity (mean \pm SD, $n = 10$). h) Quantitative analysis of ALP activity of hMSCs with osteogenic induction medium for 7 days and 14 days, respectively; the ALP activity was normalized against the μ mol/assay time/mg protein (mean \pm SD, $n = 6$); i) quantitative analysis of calcium deposition assay with osteogenic induction medium after 14 days and 21 days of culture, respectively (mean \pm SD, $n = 6$), $**p < 0.01$. NS, not significant.

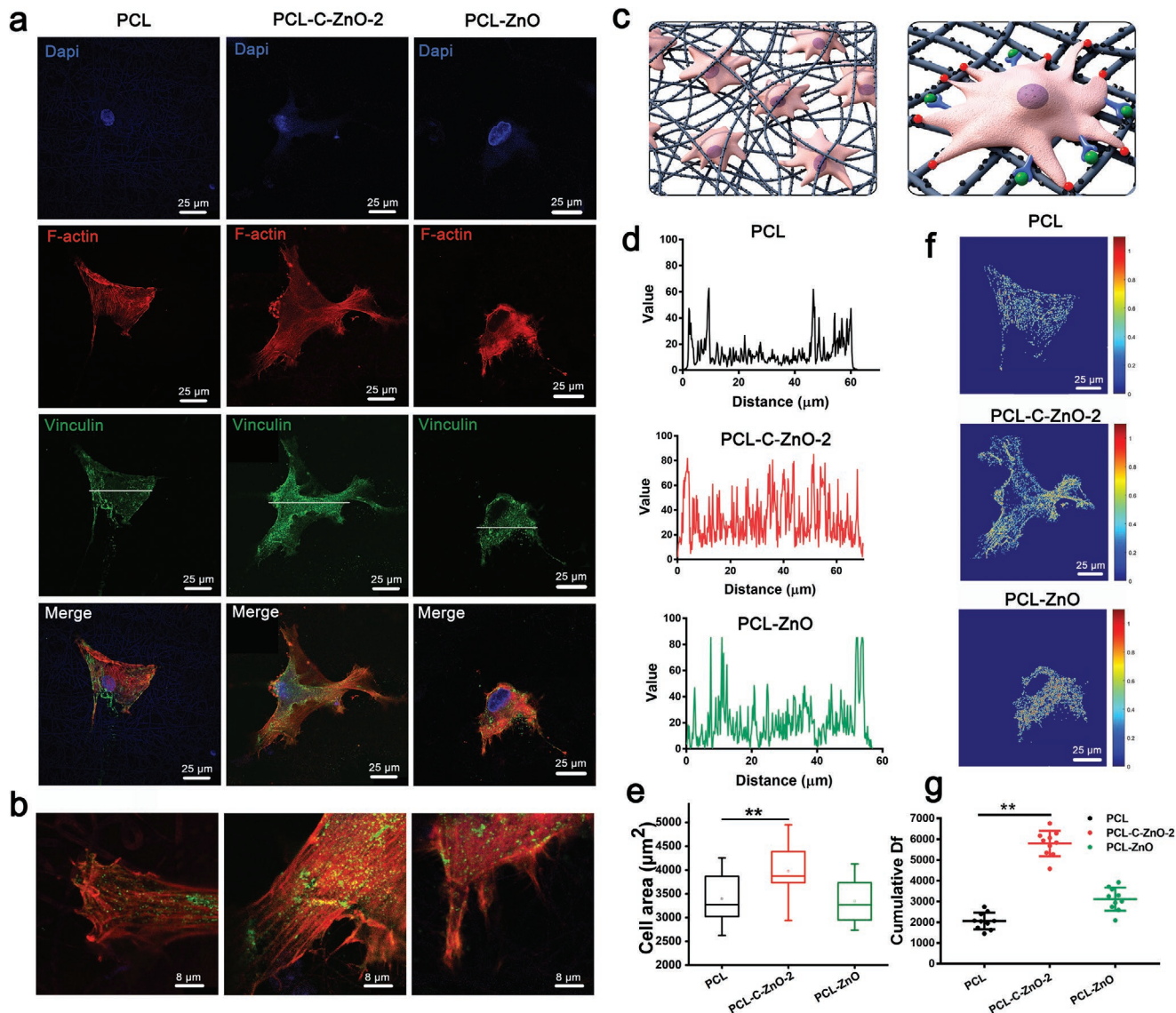


Figure 4. a) Confocal image of hMSCs growth on samples in growth medium; cells were stained with nuclei (blue), vinculin (green), and F-actin (red). b) Amplified confocal cell images in (a). c) Schematic illustration of scaffolds with nanoscale architectures on the fiber surface have larger surface area and thus providing more binding sites for protein to adsorb. d) The vinculin intensity distribution profiles along the white line based on the immunostaining image in (a) on sample PCL, PCL-C-ZnO-2, and PCL-ZnO, respectively. e) Quantitative analysis of the cell spreading area on different samples ($n = 50$). f) Matlab analysis of the 2D fractal dimension (Df) based on F-actin staining. g) Statistic quantification of the cell area according to the F-actin staining and cumulative Df value of a cell ($n = 10$). $**p < 0.01$.

nanomaterials can offer more binding sites for FAs to promote cell adhesion and motility. According to the SEM images of MSCs on scaffolds (Figure S8, Supporting Information), there is more pseudopodium on the surface of PCL-C-ZnO-2 compared with bare PCL scaffold, which proves that C-ZnO nanocarbons-modified fibrous scaffolds could improve the cells adhesion.

Moreover, correlative cell area analysis (Figure 4e) showed that the hMSCs grown on a carbon nanomaterials-incorporated surface were more significant than those on pure PCL. FAs' size markedly increased on PCL-C-ZnO-2 suggesting that the cell size and shape are related to cell-scaffolds interaction and cell-cell interaction. So fractal dimension analysis was utilized

to quantify cytoskeletal spatial arrangement and density changes on different surfaces.^[12,57,58] Figure 4f suggests that the cytoskeleton arrangement was described by a fractal dimension (Df). Through investigation and quantification analysis of the cytoskeleton distribution, the Df values on PCL-C-ZnO-2 were significantly higher than those on PCL (Figure 4g). Moreover, no obvious differences were observed between PCL and PCL-ZnO. Results suggested that the cell spheroids on carbon nanomaterials-modified PCL fibers could quickly facilitate the mature FA formation and promote the cytoskeleton rearrangement, which improves the cell adhesion to the scaffolds and cell motility, thus could further lead to increase of the osteogenic differentiation.^[43]

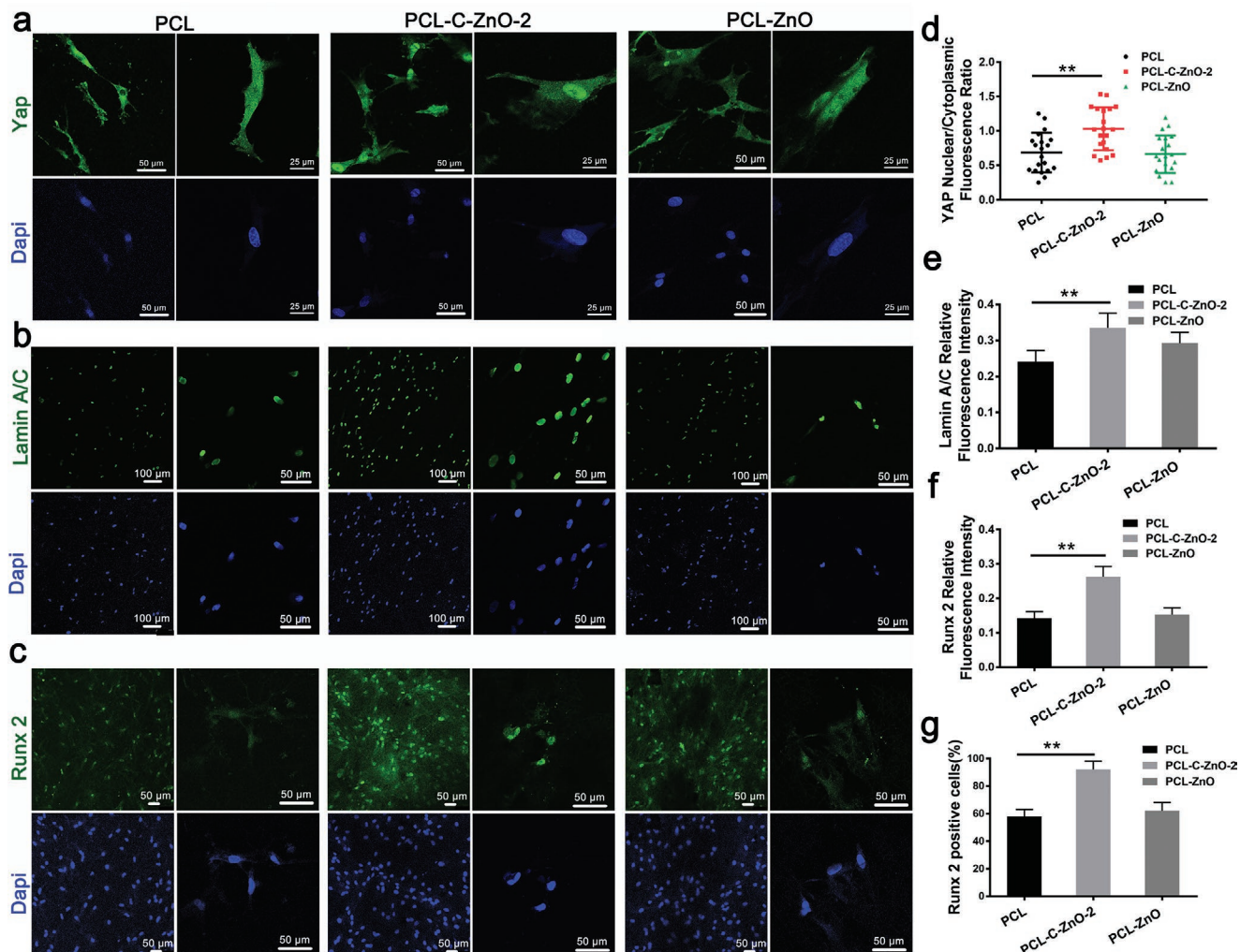


Figure 5. a) Immunofluorescence staining of the YAP signal in hMSCs for 7 days (DAPI, blue; YAP, green). b) Immunofluorescence staining of the Lamin A/C in hMSCs for 7 days (DAPI, blue; RUNX2, green). c) Immunofluorescence staining of the RUNX2 in hMSCs for 7 days in osteogenic culture medium (DAPI, blue; RUNX2, green). d) Quantitative analysis of the YAP nuclear/cytoplasmic fluorescence intensity ratio ($n = 20$). e) Relative fluorescence intensity analysis of Lamin A/C (mean \pm SD, $n = 50$); f) relative fluorescence intensity analysis of RUNX2 (mean \pm SD, $n = 50$); g) quantitative analysis of the RUNX2-positive cells percentage on different scaffolds (mean \pm SD, $n = 50$); ** $p < 0.01$, significant difference.

Many studies have shown that the cytoskeletal tension could trigger the translocation of subcellular transcriptional coactivator YAP, the successive activation of genetic signaling pathway could lead to the osteogenic specification. In this article, the role of YAP location was investigated using immunofluorescence staining of YAP in hMSC spheroids; **Figure 5a** suggests that the YAP signal on the PCL-C-ZnO-2 was more concentrated in nuclear. The statistical analysis of the nuclear/cytoplasmic ratio in **Figure 5d** suggests that the YAP protein on PCL-C-ZnO-2 was twofold more concentrated than that on PCL and PCL-ZnO, which suggested that carbon nanomaterials played an important role in the translocation of nuclear YAP. However, no obvious differences were observed between PCL and PCL-ZnO. Moreover, Lamin A/C, a protein found in the inner nuclear envelope, played a pivotal role in the interaction between nuclear events and cytoplasmic signaling. Previous results suggest that the cytoskeleton rearrangement and FA changes could alter the signal of nuclear envelope protein Lamin A/C.

This protein was stained and observed in **Figure 5b**, whereby it is found that the nuclear of the cells grown on different samples was mostly round and no obvious nuclear morphology changes could be observed. However, the relative fluorescence intensity in **Figure 5e** suggests that the increased expression of Lamin A/C on PCL-C-ZnO-2, which proves the incorporation of nanocarbons could trigger the nuclear envelope protein change. In addition, the pre-osteogenic biomarker RUNX2 was stained and observed with confocal microscopy. The fluorescent images in **Figure 5c** exhibited that the pre-osteogenic marker RUNX2 can be co-activated with YAP and Lamin A/C on PCL-C-ZnO-2. Meanwhile, the quantitative immunostaining analysis in **Figure 5f** suggests that the relative fluorescence intensity for RUNX2 on PCL-C-ZnO-2 was much stronger than that on PCL. Moreover, **Figure 5g** indicates that almost 100% of hMSCs are RUNX2 signal positive after 7 days of culture on PCL-C-ZnO; however, the RUNX2 positive cells on PCL are only around 60%. In the collection, results suggest that YAP subcellular

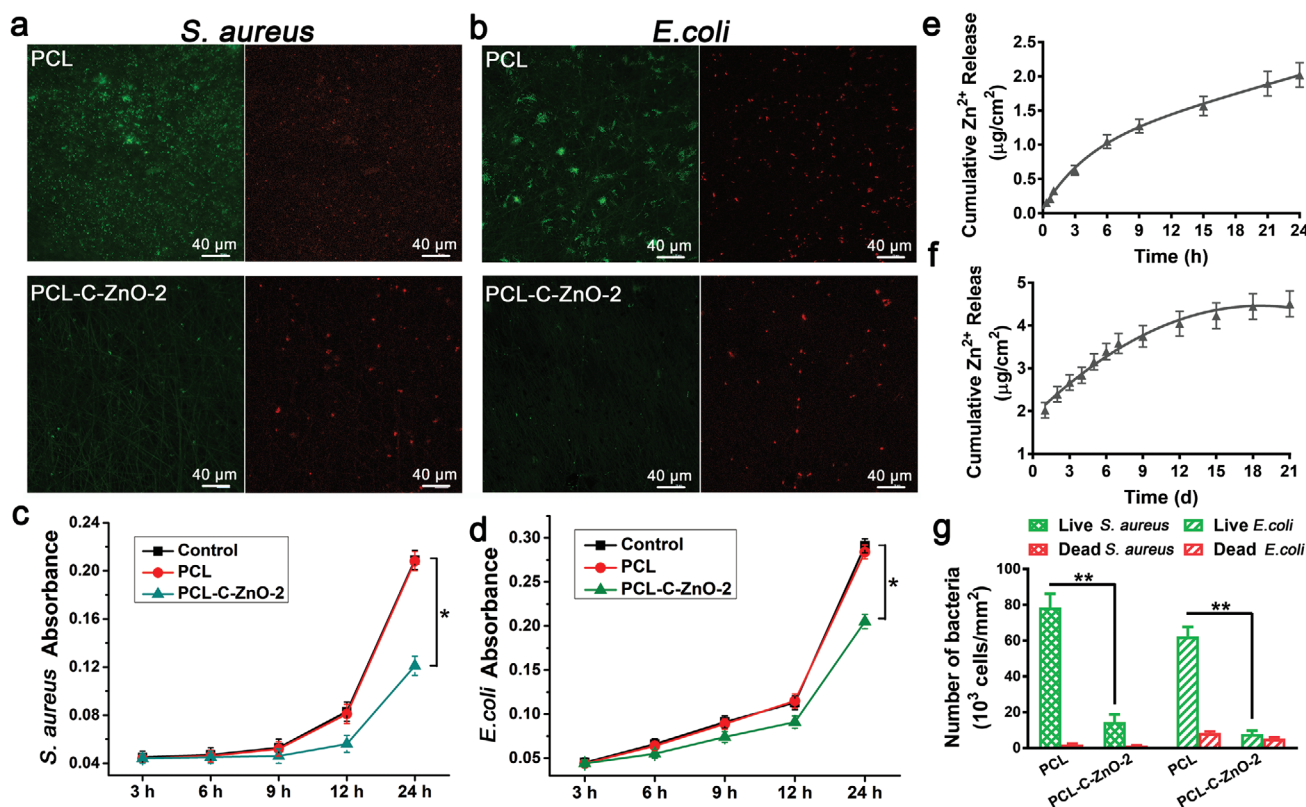


Figure 6. Live/dead staining images (red: dead, green: live) for a) *S. aureus* and b) *E. coli* after incubated with PCL and PCL-C-ZnO-2, respectively. c,d) Real-time OD₆₀₀ values with *S. aureus* and *E. coli*, respectively (mean ± SD, n = 5). e,f) Zn²⁺ ions short-term and long-term release of the PCL-C-ZnO-2. g) Quantitative analysis of live/dead bacteria numbers on the membrane. The numbers were estimated from fluorescent photographs (mean ± SD, n = 5). *p < 0.05, **p < 0.01.

localization and activity and nuclear envelope protein Lamin A/C could be influenced by carbon nanomaterials and used further to promote the expression of intranuclear RUNX2 transcription, which leads to the pre-osteogenic differentiation.

Bacterial infections accompany with scaffolds contamination are a crucial complexity primarily due to the improper delivery methods of biofactor and bacterial infections related to surgery. Supplementary implant scaffolds that could combine bacterial inhibition and osteogenic induction are of both clinical and scientific importance. In order to further investigate the antibacterial property of the C-ZnO nanocarbons modified with PCL scaffolds, gram-negative *E. coli* (ATCC 6538) and Gram-positive *S. aureus* (ATCC 25922) were chosen to perform the bacterial inhibition tests of the engineered membrane. The live/dead staining results of *S. aureus* after 12 h of incubation in Figure 6a suggest that many live bacteria grow on PCL. However, few bacteria were found on PCL-C-ZnO-2. Figure 6b shows the live/dead staining image of *E. coli* cultured on PCL-C-ZnO-2 after 6 h of incubation, it is obvious that the incorporation of C-ZnO nanoparticles endows the membrane with bacterial inhibition properties. However, bare PCL failed to show any antibacterial property, as the live bacteria grow quickly on the surface. Meanwhile, the statistical analysis of live dead cell numbers on the scaffolds in Figure 6g suggests that live *S. aureus* and *E. coli* numbers on PCL are around fourfolds and fivefolds larger than that on PCL-C-ZnO-2, respectively.

To further investigate the antibacterial property in medium, we tested the bacterial growth concentration along with time. As is shown in Figure 6c,d, when co-cultured with PCL-C-ZnO-2, the concentration increased along with bacterial growth in the medium, which was much slower than that with PCL and pure medium. After co-culture for 24 h, the amount of *S. aureus* and *E. coli* in PCL co-cultured medium was around two-folds and 1.5-folds more significant than that in PCL-C-ZnO-2 co-cultured medium, respectively. The bacterial concentration in the sample co-cultured medium suggests that PCL-C-ZnO-2 has not only bacterial inhibition properties on its surface but also exhibits antibacterial property in the surrounding environment. To verify the release capabilities of Zn²⁺ ions, the long-term and short-term release of Zn²⁺ ions of PCL-C-ZnO-2 were characterized (Figure 6e,f). During the first 6 h, Zn²⁺ ions release was very fast and the subsequent release rates were slowing down moderately. The release of Zn²⁺ ions plays a pivotal role in both bacterial killing and osteogenic differentiation.

3. Conclusion

In summary, we have constructed a novel nanocarbon-structured fibrous scaffold for stem cell-based osteogenic differentiation, which combines both physical characteristics (nanotopography) and chemical characteristics (gradual

release of the Zn²⁺ ions) in promoting osteogenic differentiation. The C-ZnO-modified scaffolds show enhanced expression of ALP, IBSP, vinculin, and a larger cell spreading area. The following nuclear translocation of YAP, improved expression of Lamin A/C and RUNX-2 signaling indicate the important role of the C-ZnO nanocarbons in promoting osteogenic differentiation. Meanwhile, the caging of ZnO nanoparticles can allow the slow release of Zn²⁺ ions, which not only activate various signaling pathways to guide osteogenic differentiation but also prevent the potential bacterial infection during implantable applications. Overall, this study may provide new insight for designing stem cells-based nanostructured fibrous scaffolds with simultaneously enhanced osteogenic and anti-infective capabilities.

Supporting Information

Supporting Information is available from the Wiley Online Library or from the author.

Acknowledgements

This work was financially sponsored by the National Key R&D Program of China (2019YFA0110600, 2019YFA0110601) and Deutsche Forschungsgemeinschaft (DFG) through grants from the Collaborative Research Center (SFB) 765. Y.X. and X.F. acknowledge the support from China Scholarship Council (CSC). C.C. acknowledges the support of the State Key Laboratory of Polymer Materials Engineering (No. sklpme2019-2-03), the Science and Technology Project of Sichuan Province (nos. 2020YFH0087 and 2020YJ0055), Fundamental Research Funds for the Central Universities, Thousand Youth Talents Plan, Alexander von Humboldt Fellowship, Special Funds for Prevention and Control of COVID-19 of SKLFPM, Donghua University (YJ202005) and Sichuan University (2020scunCoV-YJ-20005), and DRS POINT Fellowship. L.L. thanks the support of Key Laboratory of Emergency and Trauma, Ministry of Education (No. KLET-201907). Dr. Pamela Winchester is sincerely acknowledged for language polishing the manuscript. The authors acknowledge the assistance of the Core Facility BioSupraMol in Freie Universität Berlin and the bacterial lab at Sichuan University. The authors also acknowledge their laboratory members for their generous help. Open access funding enabled and organized by Projekt DEAL.

Conflict of Interest

The authors declare no conflict of interest.

Keywords

anti-infective surfaces, carbon nanomaterials, metal-organic frameworks, nanostructured fibrous scaffolds, osteogenic surfaces, stem cells

Received: May 13, 2020

Revised: July 4, 2020

Published online: August 19, 2020

[1] C. M. Madl, S. C. Heilshorn, H. M. Blau, *Nature* **2018**, *557*, 335.

[2] A. Trounson, C. McDonald, *Cell Stem Cell* **2015**, *17*, 11.

- [3] S. Pina, J. M. Oliveira, R. L. Reis, *Adv. Mater.* **2015**, *27*, 1143.
- [4] C. M. Curtin, G. M. Cuniffe, F. G. Lyons, K. Bessho, G. R. Dickson, G. P. Duffy, F. J. O'Brien, *Adv. Mater.* **2012**, *24*, 749.
- [5] A. Nasajpour, S. Ansari, C. Rinoldi, A. S. Rad, T. Aghaloo, S. R. Shin, Y. K. Mishra, R. Adelung, W. Swieszkowski, N. Annabi, A. Khademhosseini, A. Moshaverinia, A. Tamayol, *Adv. Funct. Mater.* **2018**, *28*, 1703437.
- [6] K. Huo, X. Zhang, H. Wang, L. Zhao, X. Liu, P. K. Chu, *Biomaterials* **2013**, *34*, 3467.
- [7] H. Yoshimoto, Y. M. Shin, H. Terai, J. P. Vacanti, *Biomaterials* **2003**, *24*, 2077.
- [8] N. S. Yadavalli, D. Asheghali, A. Tokarev, W. Zhang, J. Xie, S. Minko, *Small* **2020**, *16*, 1907422.
- [9] X. Wang, B. Ding, B. Li, *Mater. Today* **2013**, *16*, 229.
- [10] T. C. von Erlach, S. Bertazzo, M. A. Wozniak, C.-M. Horejs, S. A. Maynard, S. Attwood, B. K. Robinson, H. Autefage, C. Kallepitis, A. del Río Hernández, C. S. Chen, S. Goldoni, M. M. Stevens, *Nat. Mater.* **2018**, *17*, 237.
- [11] M. F. Pittenger, A. M. Mackay, S. C. Beck, R. K. Jaiswal, R. Douglas, J. D. Mosca, M. A. Moorman, D. W. Simonetti, S. Craig, D. R. Marshak, *Science* **1999**, *284*, 143.
- [12] J. Zhang, H. Yang, B. E. Abali, M. Li, Y. Xia, R. Haag, *Small* **2019**, *15*, 1901920.
- [13] Y. Hou, W. Xie, L. Yu, L. C. Camacho, C. Nie, M. Zhang, R. Haag, Q. Wei, *Small* **2020**, *16*, 1905422.
- [14] L. Li, J. Eyckmans, C. S. Chen, *Nat. Mater.* **2017**, *16*, 1164.
- [15] J. E. Frith, G. D. Kusuma, J. Carthew, F. Li, N. Cloonan, G. A. Gomez, J. J. Cooper-White, *Nat. Commun.* **2018**, *9*, 257.
- [16] X. Zhang, J. Nie, X. Yang, Z. Liu, W. Guo, J. Qiu, S. Wang, X. Yu, Y. Guan, H. Liu, L. Li, *Appl. Mater. Today* **2018**, *10*, 164.
- [17] E. S. Place, J. H. George, C. K. Williams, M. M. Stevens, *Chem. Soc. Rev.* **2009**, *38*, 1139.
- [18] A. Higuchi, Q.-D. Ling, Y. Chang, S.-T. Hsu, A. Umezawa, *Chem. Rev.* **2013**, *113*, 3297.
- [19] J. Zhang, C. Cheng, J. L. Cuellar-Camacho, M. Li, Y. Xia, W. Li, R. Haag, *Adv. Funct. Mater.* **2018**, *28*, 1804773.
- [20] C. Yang, M. W. Tibbitt, L. Basta, K. S. Anseth, *Nat. Mater.* **2014**, *13*, 645.
- [21] J. Lee, A. A. Abdeen, D. Zhang, K. A. Kilian, *Biomaterials* **2013**, *34*, 8140.
- [22] K. Alberti, R. E. Davey, K. Onishi, S. George, K. Salchert, F. P. Seib, M. Bornhäuser, T. Pompe, A. Nagy, C. Werner, P. W. Zandstra, *Nat. Methods* **2008**, *5*, 645.
- [23] S. W. Crowder, V. Leonardo, T. Whittaker, P. Papathanasiou, M. M. Stevens, *Cell Stem Cell* **2016**, *18*, 39.
- [24] M. J. Dalby, M. J. P. Biggs, N. Gadegaard, G. Kalna, C. D. W. Wilkinson, A. S. G. Curtis, *J. Cell. Biochem.* **2007**, *100*, 326.
- [25] Y. Hou, L. Yu, W. Xie, L. C. Camacho, M. Zhang, Z. Chu, Q. Wei, R. Haag, *Nano Lett.* **2020**, *20*, 748.
- [26] R. Kumar, A. Bonicelli, S. Sekula-Neuner, A. C. B. Cato, M. Hirtz, H. Fuchs, *Small* **2016**, *12*, 5330.
- [27] M. J. Landry, F.-G. Rollet, T. E. Kennedy, C. J. Barrett, *Langmuir* **2018**, *34*, 8709.
- [28] M. J. Landry, K. Gu, S. N. Harris, L. Al-Alwan, L. Gutsin, D. De Biasio, B. Jiang, D. S. Nakamura, T. C. Corkery, T. E. Kennedy, C. J. Barrett, *Macromol. Biosci.* **2019**, *19*, 1900036.
- [29] J. Xue, T. Wu, J. Li, C. Zhu, Y. Xia, *Angew. Chem., Int. Ed.* **2019**, *58*, 3948.
- [30] R. J. Wade, E. J. Bassin, W. M. Gramlich, J. A. Burdick, *Adv. Mater.* **2015**, *27*, 1356.
- [31] C. S. Hansel, S. W. Crowder, S. Cooper, S. Gopal, M. João Pardelha da Cruz, L. de Oliveira Martins, D. Keller, S. Rothery, M. Becce, A. E. G. Cass, C. Bakal, C. Chiappini, M. M. Stevens, *ACS Nano* **2019**, *13*, 2913.

- [32] Y. Hou, W. Xie, K. Achazi, J. L. Cuellar-Camacho, M. F. Melzig, W. Chen, R. Haag, *Acta Biomater.* **2018**, *77*, 28.
- [33] J. Deng, C. Zhao, J. P. Spatz, Q. Wei, *ACS Nano* **2017**, *11*, 8282.
- [34] A. J. Andersen, J. T. Robinson, H. Dai, A. C. Hunter, T. L. Andresen, S. M. Moghimi, *ACS Nano* **2013**, *7*, 1108.
- [35] T. Zhang, N. Li, K. Li, R. Gao, W. Gu, C. Wu, R. Su, L. Liu, Q. Zhang, J. Liu, *Carbon* **2016**, *105*, 233.
- [36] X. Zhou, M. Nowicki, H. Cui, W. Zhu, X. Fang, S. Miao, S.-J. Lee, M. Keidar, L. G. Zhang, *Carbon* **2017**, *116*, 615.
- [37] Y. Xia, S. Li, C. Nie, J. Zhang, S. Zhou, H. Yang, M. Li, W. Li, C. Cheng, R. Haag, *Appl. Mater. Today* **2019**, *16*, 518.
- [38] S. Marchesan, K. Kostarelos, A. Bianco, M. Prato, *Mater. Today* **2015**, *18*, 12.
- [39] C. Cheng, J. Zhang, S. Li, Y. Xia, C. Nie, Z. Shi, J. L. Cuellar-Camacho, N. Ma, R. Haag, *Adv. Mater.* **2018**, *30*, 1705452.
- [40] C. Cheng, S. Li, A. Thomas, N. A. Kotov, R. Haag, *Chem. Rev.* **2017**, *117*, 1826.
- [41] M. M. Stevens, J. H. George, *Science* **2005**, *310*, 1135.
- [42] J. Swift, I. L. Ivanovska, A. Buxboim, T. Harada, P. C. D. P. Dingal, J. Pinter, J. D. Pajerowski, K. R. Spinler, J.-W. Shin, M. Tewari, F. Rehfeldt, D. W. Speicher, D. E. Discher, *Science* **2013**, *341*, 1240104.
- [43] R. McBeath, D. M. Pirone, C. M. Nelson, K. Bhadriraju, C. S. Chen, *Dev. Cell* **2004**, *6*, 483.
- [44] L. Hanson, W. Zhao, H.-Y. Lou, Z. C. Lin, S. W. Lee, P. Chowdary, Y. Cui, B. Cui, *Nat. Nanotechnol.* **2015**, *10*, 554.
- [45] T. O. Ihalainen, L. Aires, F. A. Herzog, R. Schwartlander, J. Moeller, V. Vogel, *Nat. Mater.* **2015**, *14*, 1252.
- [46] D.-H. Kim, D. Wirtz, *Biomaterials* **2015**, *48*, 161.
- [47] J. Yang, Y. W. Yang, *Small* **2020**, *16*, 1906846.
- [48] S. Keskin, S. Kizilel, *Ind. Eng. Chem. Res.* **2011**, *50*, 1799.
- [49] C. He, D. Liu, W. Lin, *Chem. Rev.* **2015**, *115*, 11079.
- [50] J. Zhuang, C.-H. Kuo, L.-Y. Chou, D.-Y. Liu, E. Weerapana, C.-K. Tsung, *ACS Nano* **2014**, *8*, 2812.
- [51] M. Yu, D. You, J. Zhuang, S. Lin, L. Dong, S. Weng, B. Zhang, K. Cheng, W. Weng, H. Wang, *ACS Appl. Mater. Interfaces* **2017**, *9*, 19698.
- [52] P. Horcajada, R. Gref, T. Baati, P. K. Allan, G. Maurin, P. Couvreur, G. Férey, R. E. Morris, C. Serre, *Chem. Rev.* **2012**, *112*, 1232.
- [53] B. H. Neufeld, M. J. Neufeld, A. Lutzke, S. M. Schweickart, M. M. Reynolds, *Adv. Funct. Mater.* **2017**, *27*, 1702255.
- [54] X. Fan, F. Yang, J. Huang, Y. Yang, C. Nie, W. Zhao, L. Ma, C. Cheng, C. Zhao, R. Haag, *Nano Lett.* **2019**, *19*, 5885.
- [55] Y. Yang, Y. Deng, J. Huang, X. Fan, C. Cheng, C. Nie, L. Ma, W. Zhao, C. Zhao, *Adv. Funct. Mater.* **2019**, *29*, 1900143.
- [56] J. Xue, T. Wu, Y. Dai, Y. Xia, *Chem. Rev.* **2019**, *119*, 5298.
- [57] W. Qian, L. Gong, X. Cui, Z. Zhang, A. Bajpai, C. Liu, A. B. Castillo, J. C. M. Teo, W. Chen, *ACS Appl. Mater. Interfaces* **2017**, *9*, 41794.
- [58] G. Alhussein, A. Shanti, I. A. H. Farhat, S. B. H. Timraz, N. S. A. Alwahab, Y. E. Pearson, M. N. Martin, N. Christoforou, J. C. M. Teo, *Cytoskeleton* **2016**, *73*, 221.